



Contents lists available at ScienceDirect

Arabian Journal of Chemistry

journal homepage: www.sciencedirect.com



Original article

Chemical deposition from a liquid crystal template: A highly active mesoporous nickel phosphate electrocatalyst for hydrogen green production via urea electro-oxidation in an alkaline solution



Weam A. Al-Sulmi^a, Mohamed A. Ghanem^{a,*}, Saba A. Aladeemy^b, Abdullah M. Al-Mayouf^a, Nouf H. Alotaibi^a

^aChemistry Department, College of Science, King Saud University, Riyadh 11451, Saudi Arabia

^bChemistry Department, College of Science and Humanities, Prince Sattam Bin Abdulaziz University, Al-Kharj, Saudi Arabia

ARTICLE INFO

Article history:

Received 17 April 2023

Accepted 12 September 2023

Available online 16 September 2023

Keywords:

Surfactant

Mesoporous nickel phosphate

Urea oxidation reaction

Liquid crystal template

Hydrogen production

ABSTRACT

Recently the urea and urinated wastewater electrolysis process has shown promising technology for hydrogen fuel green production in addition to denitrification of wastewater. However, to make the process economically valuable, the electrocatalysts nanoarchitecture, nanometer size, shape, facets, and composition need to be engineered to boost the urea oxidation reaction (UOR). This work demonstrates a simple and novel approach to the synthesis of mesoporous nickel phosphate nanoparticles (*meso*-NiPO) via chemical deposition from a surfactant liquid crystal template. Typically, the nickel ions dissolved in the aqueous domain of the hexagonal liquid crystalline phase of the Brij[®]78 template were chemically reacted with the sodium phosphate solution to precipitate the mesoporous nickel phosphate nanoarchitecture after washing up the surfactant. The physicochemical characterizations show the *meso*-NiPO exhibits an amorphous highly mesoporous structure with a higher specific surface area (43.50 m²/g) compared to the bare nickel phosphate (*bare*-NiPO, 4.26 m²/g) prepared in the absence of surfactant. The electrochemical performance of *meso*-NiPO electrocatalyst for the urea oxidation reaction in alkaline solution exhibits superior activity including a lower oxidation onset potential (0.30 V vs. Ag/AgCl), charge transfer resistance (3.35 Ω) and mass activity of 700.7 mA/cm² mg at the oxidation potential of 0.6 V vs. Ag/AgCl. Moreover, the *meso*-NiPO reveals long-term stability, and 97.5% of the steady-state oxidation current was maintained after the 3-hour urea electrolysis test. Using an H-shape urea electrolyzer, the corresponding cathodic hydrogen production rate reached 415 μmol/h and a Faradic efficiency of 96.8 % at an applied bias of 2.0 V. The electroactivity high performance of the mesoporous nickel phosphate is ascribed to the high specific surface area and mesoporous architecture that provide efficient charge transfer, as well as mass transport of the electroactive species. The chemical deposition from a surfactant liquid crystal template has the advantages of a one-pot template, applicable to the synthesis of a wide range of nanomaterials with various compositions and nanoarchitectures at room temperature for application in electrochemical energy production and storage systems.

© 2023 The Author(s). Published by Elsevier B.V. on behalf of King Saud University. This is an open access article under the CC BY-NC-ND license (<http://creativecommons.org/licenses/by-nc-nd/4.0/>).

* Corresponding author.

E-mail address: mghanem@ksu.edu.sa (M.A. Ghanem).

Peer review under responsibility of King Saud University.



Production and hosting by Elsevier

1. Introduction

Recently, the demand for renewable energy supplies has promoted the search for alternative energy sources to fossil fuels (Megía et al., 2021). Research has focused on urea and urinated wastewater electrolysis for hydrogen fuel (H₂) green production as well as the remedy of the environmental impact (Zhu et al., 2020; Hu et al., 2020). Several proposed approaches and catalysts have been suggested for urea electrolysis to produce hydrogen and denitrification of wastewater but they suffer from the limited efficiency, high costs and instability of the electrode materials

<https://doi.org/10.1016/j.arabjc.2023.105266>

1878-5352/© 2023 The Author(s). Published by Elsevier B.V. on behalf of King Saud University.

This is an open access article under the CC BY-NC-ND license (<http://creativecommons.org/licenses/by-nc-nd/4.0/>).

(Deng et al., 2022; Liu et al., 2017a, 2017b; Yan et al., 2014; Li et al., 2022). Urea electro-oxidation reaction (UOR) in an alkaline medium, as a proficient approach, has been proposed to be an economically feasible green method for producing pure H₂ at the cathode and nitrogen (N₂) and carbon dioxide (CO₂) at the anode (Boggs et al., 2009; Zhang et al., 2019). In standard conditions, hydrogen production via urea electrolysis occurs at an overpotential of 0.37 V which is thermodynamically more favorable than the water splitting potential of 1.23 V and produces approximately 70% cheaper hydrogen fuel (Yan et al., 2014; Li et al., 2022; Boggs et al., 2009). However, the UOR kinetics are slow which may restrict the use of urea fuel in large-scale and industrial H₂ green production. Consequently, various catalysts of noble and earth-abundant-based electrodes have been employed to overcome the sluggish kinetics and inefficient urea electrooxidation (Deng et al., 2022; Liu et al., 2017a, 2017b; Yan et al., 2014; Li et al., 2022; Boggs et al., 2009; Zhang et al., 2019; Xie et al., 2018; Liu et al., 2017a, 2017b; Xie et al., 2017).

The nickel-containing nanomaterials have been widely investigated as efficient alternatives for the noble-metals electrocatalysts for small molecule oxidation, especially methanol and urea oxidation reactions in alkaline solution (Babar et al., 2021; Wu et al., 2021; Ye et al., 2018; Shen et al., 2020; Sun et al., 2021; Qian et al., 2020; Wu et al., 2020). However, to enhance the catalytic performance of Ni-based catalysts for urea electro-oxidation in an alkaline medium and make the process more economically valuable and effective for hydrogen green production, two main strategies have been employed. Firstly, increasing the specific electroactive surface and enhancing the reaction current density via using nanostructured porous electrodes (Ghanem et al., 2017; Barakat et al., 2016; Ding et al., 2016a, 2016b; Ding et al., 2014). Secondly is to synthesize nickel-based alloys and compounds with multifunctional redox systems such as Ni–Co (Ding et al., 2016a, 2016b; Ding, et al., 2014; Sun, et al., 2020), Ni–Zn (Yan, et al., 2012) or Ni–Carbon sponge (Ye, et al., 2015) which moderate the adsorption energy and reduce the urea oxidation overpotential. Within this context, mesoporous transition metals compounds, such as nickel phosphate, have unique properties that make them suitable for catalyzing the hydrogen production process and energy conversion applications (Hassaninejad-Darzi et al., 2016; Omar et al., 2018; Omar et al., 2016; Pujari et al., 2021; Zhou et al., 2019; Nwodo et al., 2023; Aziam et al., 2020; Saravanakumar et al., 2020). Song et al. prepared various mesoporous nanoarchitectures (nanotubes, nanosheets and nanocrystals) of nickel phosphate (NiPO) using different preparation methods (Song et al., 2017), showing that the porous NiPO with a nanosheet morphology catalyst exhibits the highest mass activity of 600 mA/cm² mg at 0.5 V vs. Ag/AgCl and superior durability for UOR in 1.0 M KOH. Similarly, Tsai and Wu et al. developed highly porous and crystalline zeolitic nickel phosphate nanorods by a hydrothermal route for urea oxidation in an alkaline solution (Tsai and Wu, 2020). The nickel phosphate nanorods had a better electrocatalytic performance for UOR in alkaline media compared to the corresponding Ni(OH)₂ electrode, achieving a lower onset potential of 0.27 V and higher urea-specific activity of 160 mA/cm². Moreover, Yang et al. (Yang et al., 2019) synthesized NiCoPO electrocatalysts for methanol and UOR in an alkaline solution, reporting that the introduction of Co into the NiPO matrix led to an effective increase in the anodic current and a decrease in the onset potential by 0.135 V. Interestingly, Sha et al. (Sha et al., 2019) grew NiCo₂O₄ nanowires on a nickel foam substrate by a hydrothermal method to produce an electrocatalyst with an excellent urea oxidation current in 5.0 M KOH due to more active sites in the 3D nanowire morphology. In addition, Ding et al. (Ding et al., 2016a, 2016b) reported mesoporous Ni-P by a solvothermal approach to obtain Ni-P nano-catalysts with a lower onset poten-

tial of 1.37 V vs. RHE and good urea oxidation currents of 70 mA/cm² which is better than the pure Ni nano-catalysts under similar conditions.

Within this context, our research group has reported the precipitation of a mesoporous cobalt phosphate (*meso*-CoPi) electrocatalyst from a liquid crystal template in ambient conditions (Al-Sharif et al., 2020) for enhancing the methanol oxidation in alkaline solution. The *meso*-CoPi structure comprises cobalt-oxo/hydroxophosphate and metallic cobalt layers that enhanced methanol oxidation at an overpotential of < 1.2 V vs. RHE with more than a 20-fold current increase at 1.4 V RHE compared to the bulk-CoPi counterpart prepared in absence of surfactant. The methanol oxidation activity boosting at *meso*-CoPi was credited to the specific surface area enhancement created by chemical precipitation through the liquid crystal template.

Herein, we report a novel and simple synthesis approach to prepare mesoporous nanoparticles of nickel phosphate (*meso*-NiPO) having a larger surface area (43.50 m²/g) via direct chemical precipitation within the self-assembly Birj[®]78 surfactant template at ambient conditions. The nickel ions dissolved in the aqueous domain of the hexagonal liquid crystalline phase of the Brij[®]78 template were directly reacted with sodium phosphate solution to precipitate the mesoporous nickel phosphate compound. Various techniques including XRD, BET, EDX, scanning and transmission electron microscope were employed to characterize the deposited *meso*-NiPO materials. The electrocatalytic performance of mesoporous NiP toward the oxidation of urea is evaluated through various electrochemical techniques, including cyclic voltammetry (CV), chronoamperometry (CA), and electrochemical impedance spectroscopy (EIS), measurements. The influence of factors such as catalyst loading, urea concentration, and KOH concentration on the electrocatalytic activity and stability are studied to optimize the catalyst's performance. The electrochemical behaviour and the electrocatalytic performance and stability of the mesoporous nickel phosphate nanoparticles in UOR in alkaline conditions were investigated by cyclic voltammetry, chronoamperometry and electrochemical impedance spectroscopy. The *meso*-NiPO catalyst shows significant urea oxidation enhancement with lower charge transfer resistance and higher mass activity compared to the bare nickel phosphate (*bare*-NiPO) prepared in the absence of surfactant. The synthesis approach opens a new opportunity to prepare new mesoporous catalyst nanoarchitectures with improved activity for applications in urea fuel cells and hydrogen green production. However, there are challenges such as optimizing the synthesis conditions and catalytic properties of mesoporous compounds and improving their stability and durability under various operating conditions, need to be achieved. Additionally, scaling up the production of mesoporous catalysts to meet the growing demand for hydrogen green production technology will be crucial.

2. Materials and methods

2.1. Chemicals and materials

Nickel nitrate (Ni(NO₃)₂·6H₂O, 98.0%) was obtained from LOBA Chemie and disodium hydrogen phosphate (Na₂HPO₄·2H₂O, 98.0%) was acquired from Molekula. The nonionic surfactant polyethylene glycol octadecyl ether (Birj[®]78, C₁₈H₃₇(OCH₂CH₂)₂₀OH, 97.0%), and potassium hydroxide (KOH, 85.0%) were purchased from Sigma-Aldrich. Urea pellets were acquired from AVONCHEM Corp and all chemicals were used without further purification. The hydrophilic carbon paper substrate (HCP030) was used as a working electrode and was purchased from VECK Store (China) and carbon black Vulcan (XC-72R, Fuel store). Nafion[™] perfluori-

nated resin 5 wt% solution of 45% water mixed in aliphatic alcohols was obtained from Merck. Deionized water (resistivity of 18.2 M Ω cm) was obtained from a PURELAB[®] Flex water distillation machine to prepare all solutions.

2.2. Nickel phosphate ($Ni_3(PO_4)_2$) nanoparticle synthesis

The nanoparticles of mesoporous nickel phosphate (*meso*-NiPO) catalyst were synthesized as shown in [Scheme 1](#) via direct chemical precipitation through a self-assembled Brij[®]78 surfactant template mixed with nickel nitrate solution and followed by spraying of disodium hydrogen phosphate (1.0 M) solution. First, an excess of nickel nitrate solution (10.0 mL, 0.5 M) was mixed with the melted Brij[®]78 surfactant template (2.0 g) in an ultrasonic bath for 15 min, then the homogenous mixture was cast in a petri dish and was air-dried at room temperature (25 °C) to allow the gelation via water evaporation. After several water evaporation runs monitored by water weight loss using an analytical balance, the desired surfactant/water ratio of about 40 \pm 1.0% which corresponds to the hexagonal phase of the liquid crystal template was reached. Then, an excess of disodium hydrogen phosphate solution (5.0 mL, 1.0 M), was sprayed over the template mixture in the petri dish to begin the chemical deposition of nickel phosphate and the mixture was left overnight to complete the precipitation process. The precipitate mixture was collected in a beaker and washed several times (3–4) with plenty of deionised water/acetone mixture (ratio 1:1) to remove the surfactant. the complete removal of the surfactant. Moreover, the complete removal of the surfactant was confirmed by testing the catalyst in 2.0 M KOH by cyclic voltammetry and ensuring the maximum current was obtained for each preparation batch. Finally, the deposited product was obtained via centrifugation and dried in an oven overnight at 60 °C. No carbon contamination was detected by EDX analysis which indicates the successful removal of surfactant. For comparison, the bare catalyst (as a control material) was also prepared under the same condition but in the absence of Brij[®]78 surfactant and labelled as *bare*-NiPO.

2.3. Nickel phosphate ($Ni_3(PO_4)_2$) catalyst characterisation

The crystal structures of the *meso*-NiPO catalyst were characterized by X-ray diffraction (XRD, Rigaku Miniflex 600) with graphite monochromatized Cu(K α) radiation tube operated at 40 KV and current of 15 mA in 2 θ range of 5–90° at scan of 2°/min. The surface functionality of the *meso*-NiPO powder was identified using a Bruker (SENSOR 27) Fourier-transform infrared spectrometer (FTIR). The catalyst-specific surface area was measured using the V-Sorb 2800 Porosimetry analyzer, while the pore size and volume were estimated via the Brunauer Emmer Teller (BET) approach. The scanning electron microscope (SEM, JSM-7600F, Japan) equipped with an energy-dispersive X-ray spectroscopy (EDX) analyzer

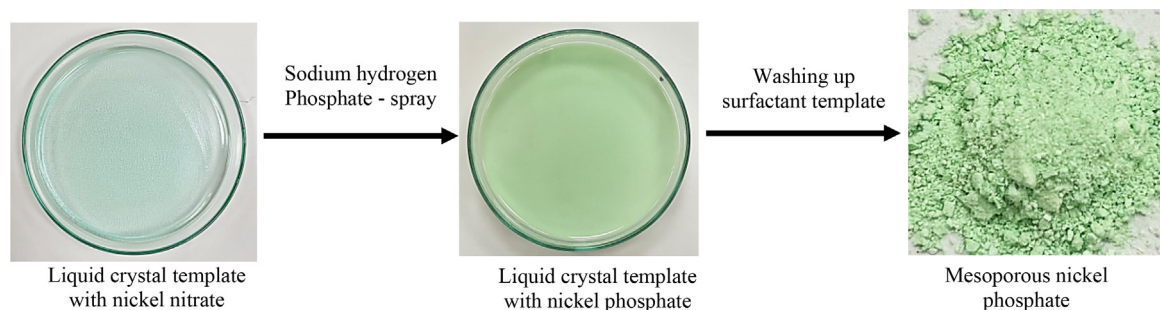
was employed to examine the surface morphology and elemental composition of the obtained mesoporous nickel phosphate powder, respectively. A transmission electron microscope (TEM, JEM 2100F) was used to study the porous and fine structure of the as-deposited nickel phosphate nanoparticles. Electrochemical measurements of the obtained mesoporous nickel phosphate nanoparticles (*meso*-NiPO) materials were performed using a biologic electrochemical workstation, including cyclic voltammetry (CV), chronoamperometry (CA), and electrochemical impedance spectroscopy (EIS) in a three-electrode glass cell. The cell consisted of a graphite sheet and Ag/AgCl as counter and reference electrodes, respectively. The working electrode was made of hydrophilic carbon paper (HCP030, 1.0 \times 1.0 cm²) loaded with *meso*-NiPO ink that was prepared by mixing 10 mg of nickel phosphate powder in 1.0 mL of deionised water/isopropanol, 10 μ L of Nafion solution (5.0 wt%), and 20 mg of carbon black (Vulcan XC-72R) in an ultrasonic bath for 60 min. The working electrode was prepared by casting the required volume of *meso*-NiPO ink on the carbon paper electrode and drying it with hot air before executing the electrochemical characterisation experiments.

The volumetric determination of the hydrogen gas production rate and the efficiency was performed using the H-shaped glass electrolyzer as shown in [Fig. S4 \(Supporting Materials\)](#) which consists of anodic and cathodic compartments connected by a central channel. The anode was made of *meso*-NiPO catalyst (about 0.50 mg/cm²) coated on both sides of carbon paper (2.0 \times 3.0 cm²) and nickel foam (2.0 \times 3.0 cm²) as a cathode. The electrolyzer was filled with 2.0 M KOH containing 0.33 M urea solution up to the zero-mark level of the cathodic compartment. The urea electrooxidation at the *meso*-NiPO anode was initiated by applying suitable bias voltage (1.6, 2.0 and 2.5 V) as controlled by the power supply, and then the bubbles of hydrogen gas started to evolve at the nickel foam cathode. As the urea electrooxidation reaction progresses, the volume of the hydrogen gas is monitored at regular intervals until a desired reaction time is achieved.

3. Results and discussion

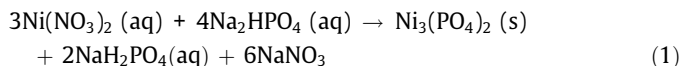
3.1. Catalyst characterisation

The mesoporous nickel phosphate nanoparticles ($Ni_3(PO_4)_2 \cdot 3H_2O$) were prepared as shown in [Scheme 1](#) via chemical precipitation from a liquid crystal template using the self-assembled Brij[®]78 surfactant. In this approach, nickel ions dissolved in the aqueous domain of the surfactant hexagonal template were chemically deposited using excess disodium hydrogen phosphate ($Na_2HPO_4 \cdot 2H_2O$) at room temperature. In a typical reaction, the $Na_2HPO_4 \cdot 2H_2O$ dissociates and releases phosphate ions which react with nickel ions within the aqueous domain of the surfactant liquid crystal template forming hydrated nickel phosphate precip-



Scheme 1. Chemical precipitation of mesoporous nickel phosphate from surfactant liquid crystal template.

itate ($\text{Ni}_3(\text{PO}_4)_2$) (Omar et al., 2018), and the balanced reaction can be represented as shown in Eq. (1).



The crystal structure of an as-synthesized mesoporous nickel phosphate catalyst is shown in Fig. 1a. The broad and low-intensity diffraction peaks indicate the amorphous/semi-crystalline nature of the deposit because the precipitation was performed in ambient conditions. However, the broad diffraction peaks at 2Θ about 7.5 , 27.8 , 35.2 , 52.2 and 62.4° can be assigned to the plane (100), (111), (311), (222), and (313) respectively, which is consistent with the structure of the hydrate $\text{Ni}_3(\text{PO}_4)_2 \cdot x\text{H}_2\text{O}$ (JCPD card no. 038–1473) (Omar et al., 2018; Omar et al., 2016;

Pujari et al., 2021). The XRD result of the *bare*-NiPO deposit is quite similar to the *meso*-NiPO one indicating both catalysts have an amorphous/semi-crystalline structure. Fig. 1b shows the amorphous *meso*-NiPO FT-IR spectra characterization along with the *bare*-NiPO catalyst. The FT-IR spectra show the presence of a strong absorption asymmetric vibration mode at 1070 cm^{-1} which is characteristic of the vibrational bond of the PO_4^{3-} group for both *meso*- and *bare*-NiPO catalysts. In addition, the peaks at 584 and 907 cm^{-1} belong to the vibration mode of the phosphate group (PO_4^{3-}) and the stretching of the P–O–P linkages, respectively, confirming the presence of the phosphate group (Klähn et al., 2004). The two characteristic bands around 3423 and 1641 cm^{-1} correspond to hydroxyl ion (O–H) stretching and a water molecule (H–O–H) bending modes (Hassaninejad-Darzi et al., 2016). Notably, the band intensities of mesoporous nickel phosphate nanopar-

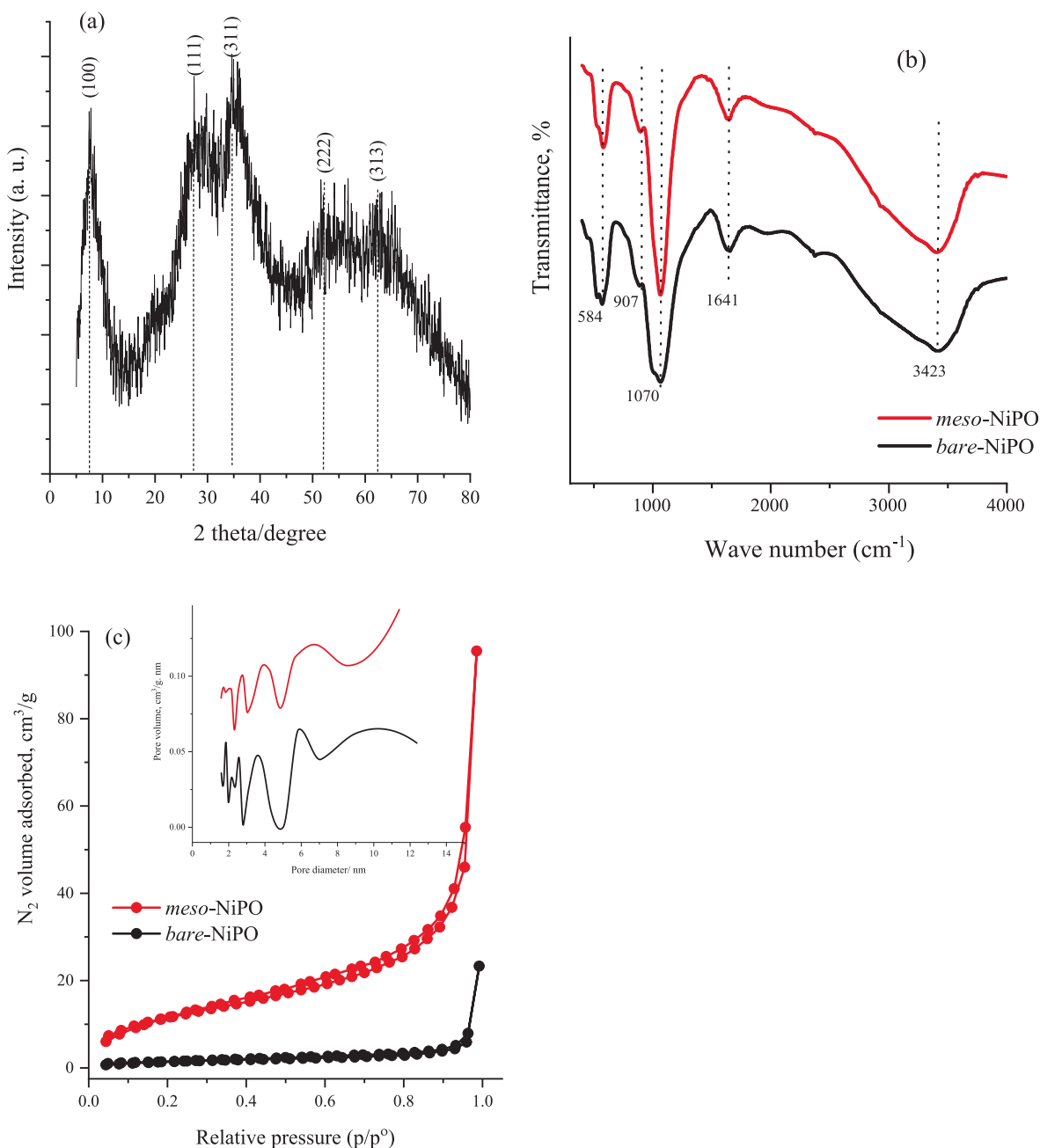


Fig. 1. (a) XRD pattern of as-deposited *meso*-NiPO nanoparticles, (b) the FT-IR spectrum of amorphous *meso*-NiPO and *bare*-NiPO catalysts, (c) N_2 gas adsorption–desorption isotherms of amorphous *meso*-NiPO and *bare*-NiPO catalysts, and the inset shows the corresponding BJH desorption pore size distribution curves.

ticles increased compared to the *bare*-NiPO catalyst, indicating that *meso*-NiPO nanoparticles have more phosphate groups and chemisorbed water, presumably due to the presence of mesoporous, structural water and a larger surface area. Fig. 1c shows the N_2 adsorption–desorption isotherms of *meso*-NiPO and *bare*-NiPO catalysts, which are classified as type IV with a hysteresis loop (Sing et al., 1985) and appeared at a higher relative pressure (p/p^0) between 0.85 and 0.95, indicating the mesoporous nature of the as-prepared materials. The BET surface area of as-deposited *meso*-NiPO and *bare*-NiPO catalysts were 43.50 and 4.26 m^2/g , respectively, confirming that the *meso*-NiPO has a ten times higher mesoporous specific surface area than the *bare*-NiPO. The inset in Fig. 1c shows the corresponding pore size distribution of the *meso*-NiPO and *bare*-NiPO catalysts with polynomial pore diameters in the range of 3.0, 4.0 and 6.5 nm. This is consistent with the TEM characterisation images in Fig. 2c below that revealed the formation of disordered and irregular pores using the soft surfactant template.

The surface morphology and bulk composition of the hydrated *meso*-NiPO ($Ni_3(PO_4)_2$) nanoparticles are shown in Fig. 2 a and b, indicating that the *meso*-NiPO deposit has “berry fruit” like morphology (inset Fig. 2b) with very small nanoparticles (20–25 nm average size) assembled into semispherical larger particles with an average size of 175 nm as shown in the inset histogram in Fig. 2a. Fig. 2c shows a lower magnification TEM image of *meso*-NiPO nanoparticles that confirms the formation of the highly mesoporous network left after the removal of the Brij[®]78 surfactant template. The high-resolution TEM microphotograph shown

in Fig. 2d indicates that the mesopore is arranged in a disordered structure with various-sized pores (≤ 5 nm) and little lattice fringes can be observed confirming its amorphous/semicrystalline structure, which is consistent with the N_2 adsorption–desorption isotherms and XRD analysis shown above. This could be due to the surfactant liquid crystal template being a soft scaffold that easily changes during the chemical precipitation of nickel phosphate within the aqueous domain of the template and the hydrophobic Brij[®]78 surfactant renders the formation of crystalline structure.

Moreover, Fig. 3 shows the EDX elemental mapping analysis of *meso*-NiPO nanoparticles confirming the presence and uniform distribution of Ni, P and O elements with the elemental composition of 48.10, 12.40, and 39.50 wt% respectively, consistent with the chemical stoichiometric of $Ni_3(PO_4)_2$ and considering an excess of oxygen due to the formation of the hydrated form of the $Ni_3(PO_4)_2$.

3.2. Electrochemical characterization of the *meso*-NiPO nanoparticles

Fig. 4a shows the cyclic voltammograms responses of the *meso*-NiPO and *bare*-NiPO catalysts loaded on the CP electrode (200 $\mu g/cm^2$) at 50 mV/s in 2.0 M KOH within the potential range from -0.20 to 0.60 V vs. Ag/AgCl. The *meso*-NiPO and *bare*-NiPO electrodes display a pair of well-defined anodic and cathodic peaks located at 0.36 and 0.25 V vs. Ag/AgCl respectively corresponding to the redox reaction of Ni(II)/Ni(III) phosphate with hydroxyl ions (OH^-) during the potential cycling forming $Ni_3(OH)_3(PO_4)_2$ according to Eq. (2) (Al-Omair et al., 2017; Touny and Saleh, 2018). Inter-

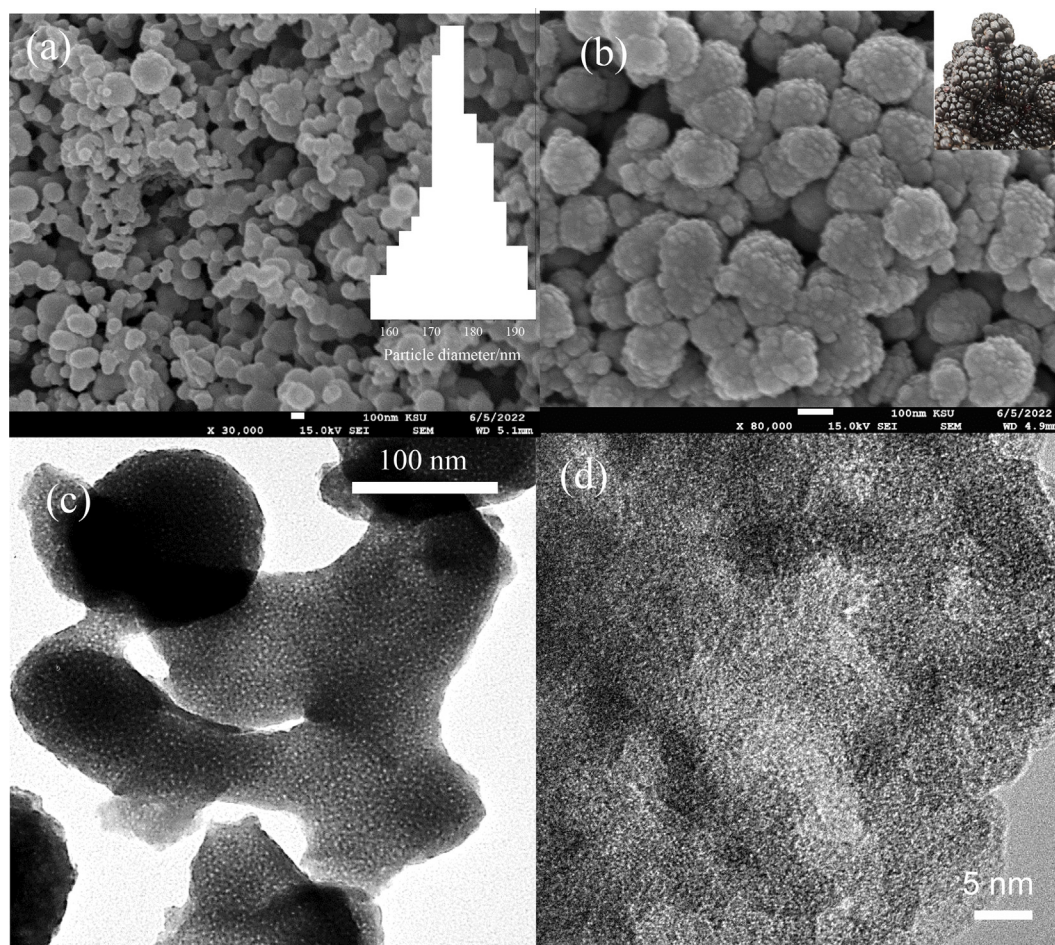


Fig. 2. (a–b) SEM images at different magnifications, the insets show the nanoparticles size histogram and berry fruit image and (c–d) TEM photographs of *meso*-NiPO catalyst at different magnifications, the yellow circles highlighted the mesopores.

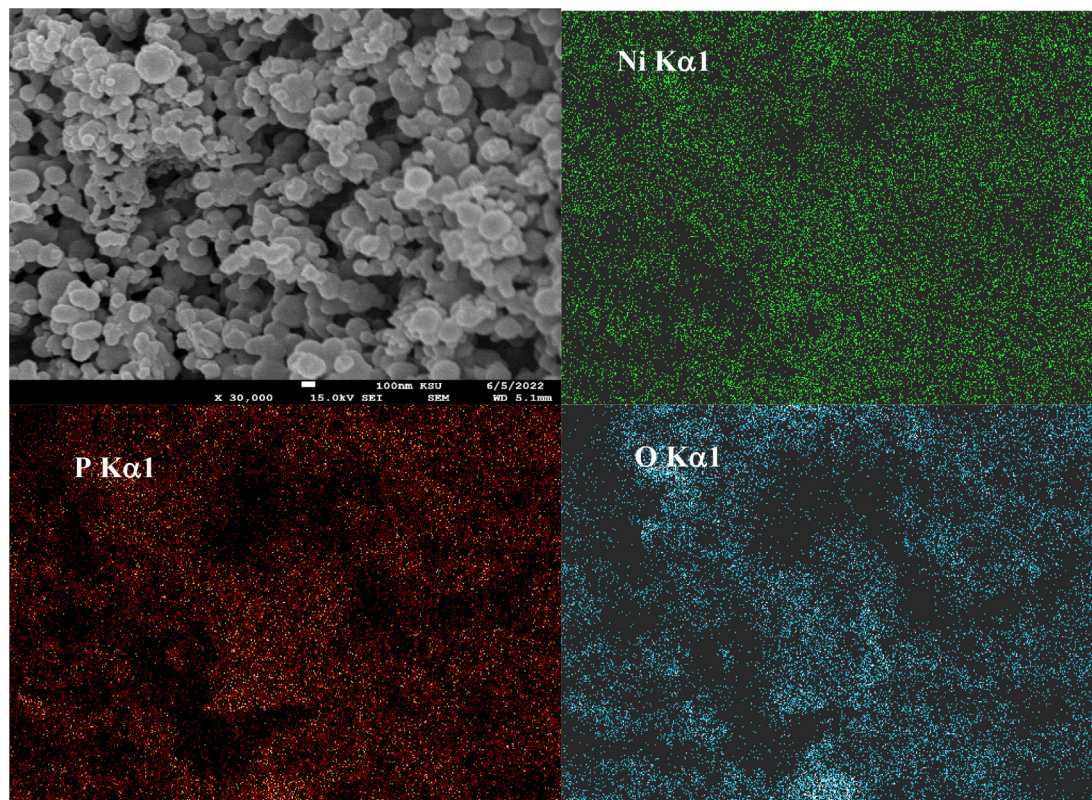


Fig. 3. EDX elemental mapping of as-prepared mesoporous nickel phosphate.

estingly, the redox peak current density at the *meso*-NiPO is more than four times higher than that recorded at the *bare*-NiPO electrode, indicating that the *meso*-NiPO catalyst has more surface area and electrochemical active sites due to the presence of mesoporous network structure. In addition, the more negative shift in the onset potential observed at the *meso*-NiPO catalyst suggests a more easy reaction with hydroxide ions according to Eq. (2).

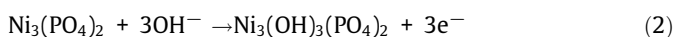


Fig. 4b shows the influence of different *meso*-NiPO loadings (20, 50, 100, 200, 300, and 400 μg) on the Ni(II)/Ni(III) redox peak currents in 2.0 M KOH at 50 mVs^{-1} . As shown in the inset in Fig. 4b, the Ni(II)/Ni(III) redox peak current density gradually increased as the *meso*-NiPO loading increased from 20 to 200 μg , then became saturated at higher loading of 300 and 400 μg . This behaviour can be attributed to an increase in the electrochemically active surface area and catalytic active sites as the catalyst loading increased. However at higher catalyst loading (>200 μg) the current density saturated or declined due to layer thickness increases at higher loading that limits hydroxide ion diffusion and accessibility to the catalyst active sites. Furthermore, the effect of various scan rates on the redox process of *meso*-NiPO nanoparticles (loading 200 μg) is shown in Fig. 4c. The CVs response shows the redox peak currents increase with the potential scan rates from 2.0 to 100 mV/s , with a linear relationship between the redox peak currents and the square root of the scan rates (inset in Fig. 4c), confirming the reaction of hydroxide ions with *meso*-NiPO nanoparticles (Eq. (3)) proceeding in a diffusion-controlled process.

Fig. 5a shows the cyclic voltammograms of the 200 $\mu\text{g}/\text{cm}^2$ of *meso*-NiPO nanoparticles electrode in the absence and presence of 0.33 M urea and 2.0 M KOH solution compared to the *bare*-NiPO electrode at 50 mV/s scan rate. The CVs response of the *meso*-NiPO catalyst in 2.0 M KOH displays anodic and cathodic

peak currents at 0.36 and 0.25 V vs. Ag/AgCl respectively corresponding to the redox transformations of Ni(II)/Ni(III) species (Hu et al., 2020; Al-Sharif et al., 2020; Klähn et al., 2004). The CVs responses of the *meso*-NiPO electrode in 0.33 M urea solution exhibit a dramatic increase in the anodic urea oxidation current at the same onset potential of 0.30 V where the Ni(II)/Ni(III) species are formed, indicating that *meso*-NiPO nanoparticles catalyse the UOR (Wu et al., 2020; Song et al., 2017; Tsai et al., 2020; Yang et al., 2019; Sha et al., 2019; Ding et al., 2016a, 2016b). The *meso*-NiPO electrode reveals significant activity enhancement toward UOR compared with the *bare*-NiPO electrode, achieving specific activity of 141.4 mA/cm^2 at a potential of 0.60 V vs. Ag/AgCl (equivalent to the mass activity of 700.7 mA/cm^2 mg) which was about 4.5-fold higher than the *bare*-NiPO electrode (31.0 mA/cm^2). The urea oxidation current enhancement at the *meso*-NiPO catalyst is attributed to the high specific surface area and mesoporous architecture that provide more active sites, efficient charge transfer, as well as higher mass transport of the electroactive species. Moreover, the *meso*-NiPO catalyst displays a UOR onset potential of 0.30 V vs. Ag/AgCl, which is lower than the onset potential of the *bare*-NiPO catalyst (0.34 V), indicating that the UOR thermodynamically is more favourable at the mesoporous structure of $\text{Ni}_3(\text{PO}_4)_2$ catalyst. As shown in the inset in Fig. 5a, the *meso*-NiPO electrode displays a Tafel slope of 20.3 m/dec which is lower than that of the *bare*-NiPO (30.2 m/dec), indicating faster kinetics and charge transfer of catalytic urea oxidation at *meso*-NiPO compared to the *bare*-NiPO catalyst. It is worth noting that the onset potential of oxygen evolution reaction in the absence of urea occurs at above 0.55 V vs. Ag/AgCl. In contrast, the urea onset oxidation potential occurs at around 0.30 V vs. Ag/AgCl which is about 0.25 V less than the oxygen evolution reaction which signifies the benefit of using urea instead of water for cheaper hydrogen green production.

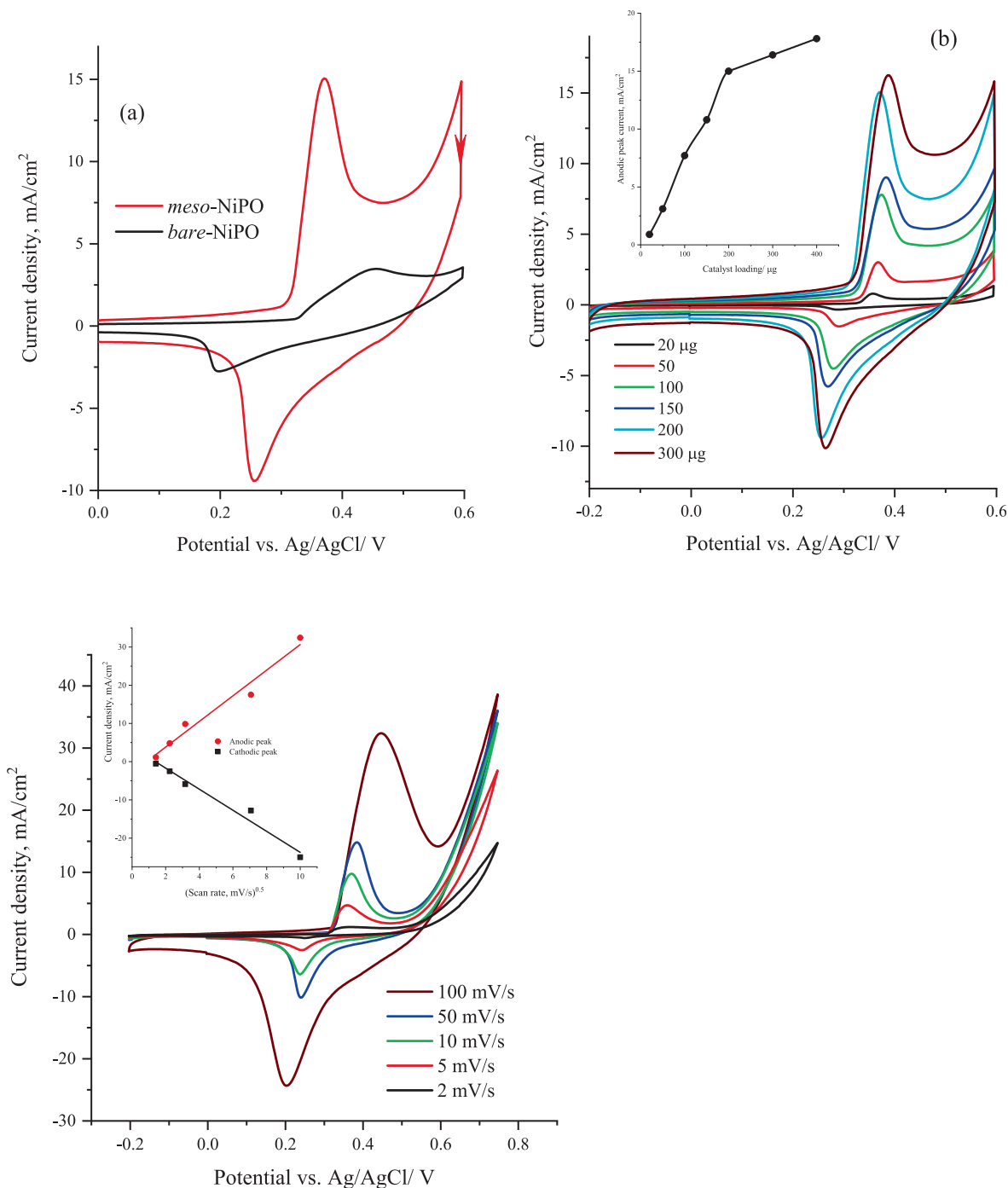


Fig. 4. (a) cyclic voltammograms responses of both *meso*-NiPO nanoparticles and *bare*-NiPO catalysts loaded on CP electrode (200 µg/cm²) at 50 mV/s in 2.0 M KOH solution, (b) cyclic voltammograms of different loadings of *meso*-NiPO in 2.0 M KOH at 50 mV/s⁻¹, the inset shows the relationship between anodic peak currents and catalyst loading, and (c) cyclic voltammograms of 200 µg/cm² of *meso*-NiPO nanoparticles at different scan rates in 2.0 M KOH, and the inset shows the relationship between peak currents and the square root of the scan rate.

Furthermore, Fig. 5b presents the CVs response of the *meso*-NiPO electrocatalyst at 50 mV/s in the 0.33 M urea at different catalyst loading from 20 to 400 µg, showing that the anodic current gradually increases with increasing the *meso*-NiPO electrocatalyst loading up to 200 µg due to the enhancement of Ni(II)/Ni(III) active sites for UOR (inset in Fig. 5b). However, the oxidation currents begin to saturate at higher loading of the *meso*-NiPO catalyst (>200 µg) because the film thickness increases and the limited accessibility and diffusion to the active sites.

Fig. 5c presents the CVs of the *meso*-NiPO electrode in 2.0 M KOH containing different concentrations of urea at 50 mV/s, showing that the oxidation currents of UOR significantly increase as the urea concentrations increase from 0.0 to 0.33 M, then the anodic current decreases at a higher urea concentration of 0.5 M, indicating that the electrochemical urea oxidation is a diffusion-controlled process at lower urea concentrations (below 0.33 M). Notably, as shown in the inset of Fig. 5c, the decrease of the urea oxidation current at a urea concentration greater than 0.33 M is

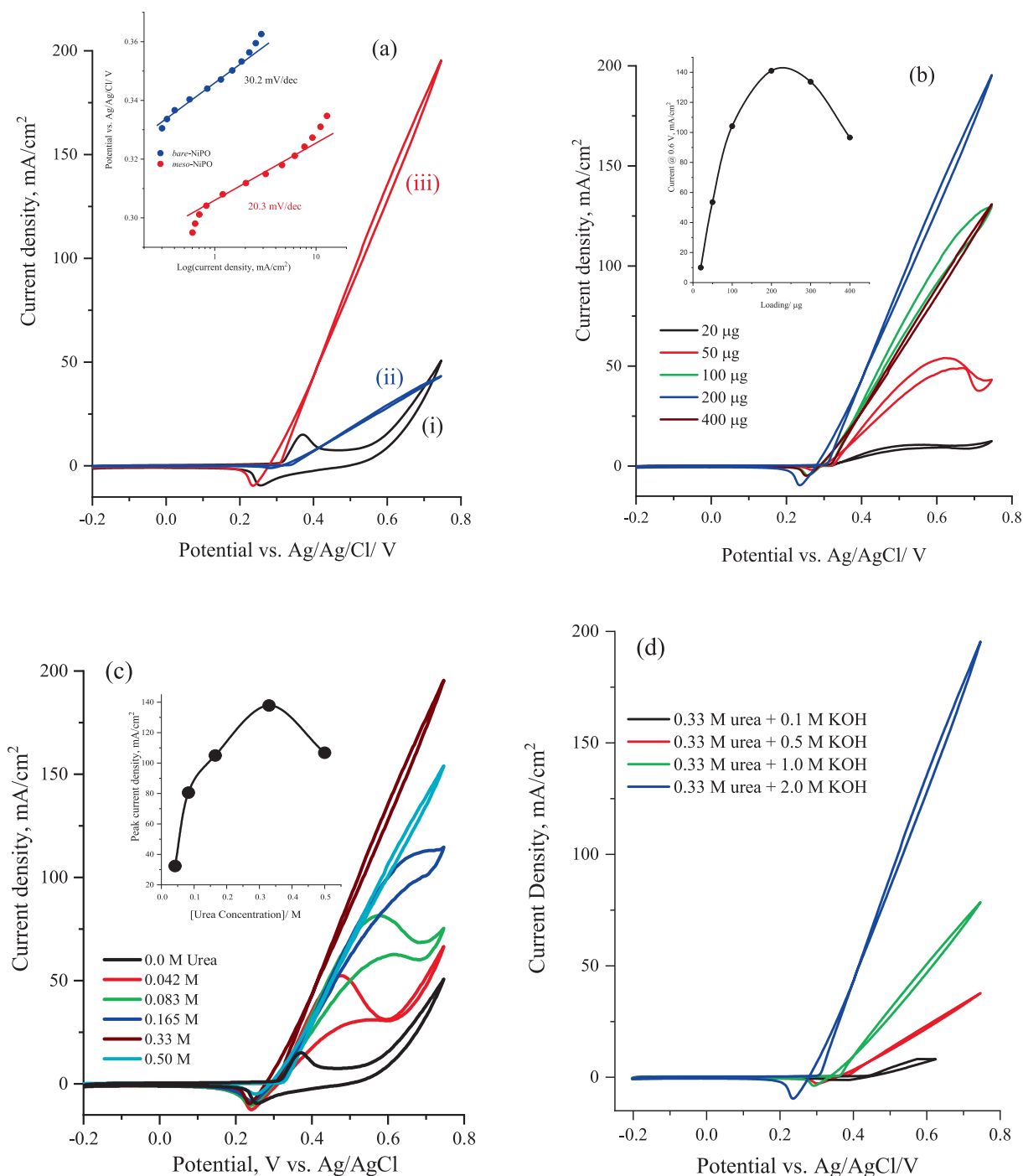
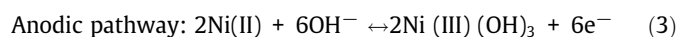
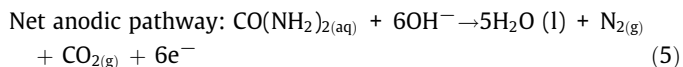
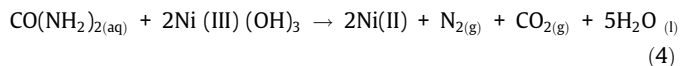


Fig. 5. (a) cyclic voltammograms at 50 mV/s of 200 $\mu\text{g}/\text{cm}^2$ of *meso*-NiPO in 2.0 M KOH (i) and in the presence of 0.33 M urea solution (iii) and compared with *bare*-NiPO (ii) catalyst; the inset shows the calculated Tafel slopes of both catalysts derived from polarization curve in Fig. 1a, (b) cyclic voltammograms at 50 mV/s for the effect of *meso*-NiPO catalyst loading in 2.0 M KOH containing 0.33 M urea, the inset is the relationship between catalyst loading and urea oxidation current at 0.6 V vs. Ag/AgCl, (c) presents the CVs of the *meso*-NiPO electrode in 2.0 M KOH containing different concentrations of urea at 50 mV/s, and the inset shows the relationship of the oxidation current density at 0.6 V vs. Ag/AgCl and the urea concentration in 2.0 M KOH solution, and (d) cyclic voltammograms of the *meso*-NiPO (200 $\mu\text{g}/\text{cm}^2$) electrode at 50 mV/s in 0.33 M urea solution containing different concentrations of KOH.

possibly attributed to some kinetic limitations toward UOR due to the competitive adsorption of hydroxyl ions with urea molecules at the mesoporous $\text{Ni}_3(\text{PO}_4)_2$ catalyst surface. Under alkaline conditions, the electrochemical oxidation of urea at nickel-based catalysts follows a catalyst-regeneration mechanism (an indirect electrochemical-chemical mechanism) as shown in Eqs. (3) to (5) (Hu et al., 2020; Al-Sharif et al., 2020; Klähn et al., 2004; Vedharathinam and Botte, 2012; Vedharathinam and Botte,

2013). The reaction mechanism pathways involved the electrooxidation of Ni(II) to Ni(III) by hydroxyl ions (Eq. (4)) within the nickel phosphate matrix, and then Ni(III)(OH)₃ chemically reacts with urea. Notably, the urea completely oxidises and Ni(II) is regenerated (Eq. (4)) and the overall anodic reaction is shown in Eq. (5) (Al-Omar et al., 2017; Vedharathinam and Botte, 2013).





The N_2 and CO_2 gases are the main urea electrooxidation products using nickel-based catalysts. However, a recent work (Hopsort et al. 2023) reported the identification of various compounds such as cyanate, ammonium, carbonate and nitrite ions that are the main byproducts of urea electrooxidation using Ni(II)/Ni(III) redox catalyst. Moreover, Fig. 5d shows the CVs of *meso-meso*-NiPO nanoparticles ($200 \mu\text{g}/\text{cm}^2$) at 50 mVs^{-1} in 0.33 M urea solution

containing different concentrations of KOH. It can be seen a substantial negative shift of urea oxidation onset potential results from the Nernst effect of the increased hydroxide ion concentration (i.e. the UOR becomes thermodynamically more favourable). Moreover, when the hydroxide ion was increased from 0.1 to 2.0 M, the urea oxidation current was increased by more than fifteen times at a more positive potential. This can be credited to the factors of the acceleration of the anodic reaction shown in Eq. (3) and the increase of the ionic strength and active site accessibility of the high surface area mesoporous film.

Fig. 6a shows the long-term stability chronoamperometry (CA) at different catalyst loadings compared to the *bare*-NiPO electrode at an applied potential of 0.6 V vs. Ag/AgCl. The chronoampero-

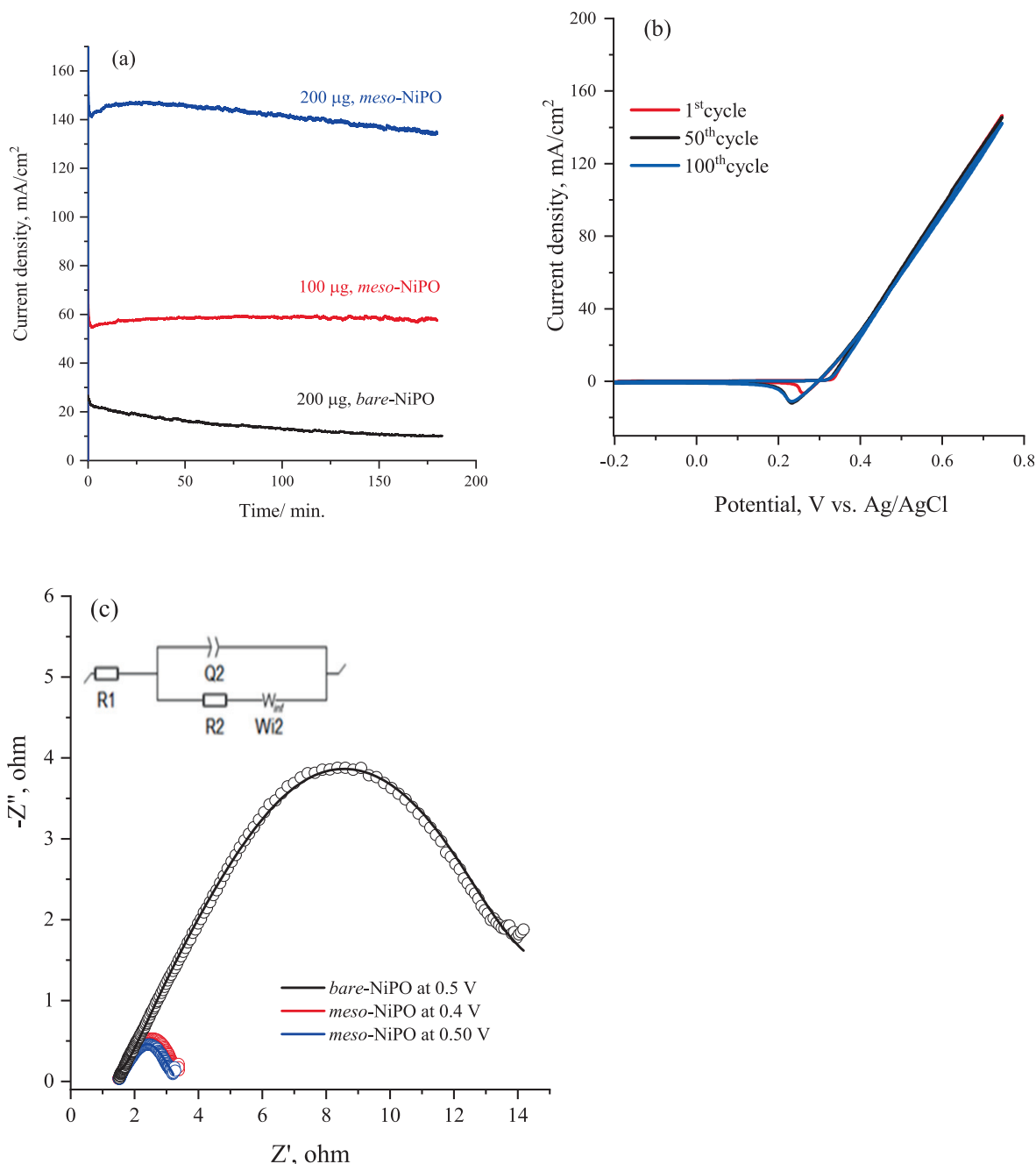


Fig. 6. (a) chronoamperograms for 3 h of *meso*-NiPO electrode with different loading and compared with *bare*-NiPO catalysts in 0.33 M urea/2.0 M KOH at the potential of 0.6 V vs. Ag/AgCl, (b) the multi-cycle responses (100 cycles) of the *meso*-NiPO electrode in 0.33 M urea solution in 2.0 M KOH at 50 mV/s and (c) Nyquist plot recorded for 200 µg/cm² of the *meso*-NiPO catalyst and *bare*-NiPi at shown potentials and frequency of 100 kHz to 10 MHz in 2.0 M KOH containing 0.33 M urea, the inset show the equivalent circuit.

grams of the *meso*-NiPO electrode exhibit a significantly higher urea steady-state oxidation current with increasing catalyst loading from 100 μg to 200 μg compared to the *bare*-NiPO electrode in 2.0 M KOH containing 0.33 M urea, which is attributed to more Ni(II)/Ni(III) active sites. Moreover, at the end of the 3-hour electrolysis, the *meso*-NiPO electrode had a higher current density (135.6 mA/cm^2) and 97.5% of the urea oxidation in 2.0 M KOH was maintained than for the *bare*-NiPO catalyst (10.4 mA/cm^2) at the same loading (200 μg), confirming the *meso*-NiPO catalyst is more active and stable for UOR in a basic solution. Furthermore, Fig. 6b presents the multi-cycle responses (100 cycles) of the *meso*-NiPO electrode in 0.33 M urea solution in 2.0 M KOH at 50 mV/s^{-1} , showing that the *meso*-NiPO catalyst displays extremely stable urea oxidation currents up to a potential of 0.70 V vs. Ag/AgCl within 100 cycles, thus superior stability for UOR in basic media.

Fig. 6c provides the Nyquist plot recorded for 200 μg of *meso*-NiPO nanoparticles compared with *bare*-NiPO catalyst at various applied potentials in 0.33 M urea/ 2.0 M KOH. Table 1 reports the EIS parameters obtained within the fitting of impedance spectra for both *meso*-NiPO and *bare*-NiPO catalysts by a suitable equivalent circuit model (inset in Fig. 6c) that consisted of a parallel combination of (Q_2) and (R_2) elements at higher frequencies and Warburg diffusion element (W_{de}) is in a series with R_2 (R_2 -W// Q_2) that are in series with solution resistance (R_1). The Q element that was used to fit the EIS results refers to the constant phase element which generally applies instead of the double-layer capacitor because of the surface inhomogeneity, porosity, roughness, and surface/normal distribution of the elements (Singh et al., 2015). The results of Nyquist plots the arc radii for the *meso*-NiPO electrode significantly decreased compared to *bare*-NiPO at the oxidation potential of 0.50 V vs. Ag/AgCl, suggesting the substantial improved UOR and faster charge transfer at the *meso*-NiPO electrode. As shown in Table 1 the the electrolyte resistance (R_1) is

practically constant at 1.48 Ω , whereas the urea oxidation charge transfer resistant (R_2) value for the *meso*-NiPO catalyst is equals 3.85 and 3.35 Ω at applied potential of 0.40 and 0.50 V respectively, which is significantly lower than that of *bare*-NiPO electrode (16.30 Ω). The impedance results confirmed the charge transfer of urea electrooxidation is much faster at the mesoporous *meso*-NiPO than *bare*-NiPO catalyst which is consistent with CVs results.

Finally, Fig. 7 reveals the surface morphology and EDX elemental analysis of the *meso*-NiPO catalyst after being used for 3 h in the stability test during the electrolysis in 0.33 M urea/ 2.0 M KOH solution at 0.60 V vs. Ag/AgCl (Fig. 7a). Interestingly, the SEM image in Fig. 7a shows that the after use *meso*-NiPO catalyst maintains the surface morphology of burry fruit nanoparticles almost similar to the as-prepared mesoporous $\text{Ni}_3(\text{PO}_4)_2$ nanoparticles (Fig. 2b). However, the EDX elemental analysis (Fig. 7b) reveals that the *meso*-NiPO elements wt. % composition changes after the catalyst was used in the stability test. The Ni content significantly decreased from 48.1 to 38.4 wt% and similarly, the P decreased from 12.4 to 6.69 wt%, whereas the oxygen content increased from 39.5 to 54.9 wt% after the *meso*-NiPO catalyst was oxidised during the stability test in an alkaline solution. This change in elemental composition is attributed to the *meso*-NiPO catalyst exposed to complex chemical and electrochemical reactions according to Eqs. (3) to (5) during the electrolysis process in 0.33 M urea/2.0 M KOH solution at 0.50 V vs. Ag/AgCl. Moreover, the N_2 and CO_2 gas products' evolution during urea electrolysis may cause mechanical leaching of the catalyst particles. Even though the *meso*-NiPO catalyst exhibits remarkable stability and maintained 97.5% of the urea steady-state oxidation current after the 3-hour stability test as shown in Fig. 4c. In addition, Table 2 reports the electrocatalytic activity of the *meso*-NiPO catalyst as compared and evaluated against the state-of-the-art nickel-based catalysts reported in the literature. The *meso*-NiPO catalyst demonstrated superior specific and mass electrocatalytic activity for urea oxida-

Table 1

EIS parameters recorded for the equivalent circuit of *meso*-NiPO compared to bar catalyst at different potentials: 0.35, 0.40, 0.45, and 0.50 V in 0.33 M urea/2.0 M KOH.

Potential vs. Ag/AgCl/V	EIS parameters			
	R_1 , ohm	Q_2 , F.S(α^{-1})	R_2 , ohm	W_{inf} , cm^2/s
<i>meso</i> -NiPO, 0.50 V	1.329	0.341	3.35	0.076
<i>meso</i> -NiPO, 0.40 V	1.413	0.254	3.85	3.286×10^{-2}
<i>bare</i> -NiPO, 0.5 V	1.519	0.027	16.3	0.538×10^{-3}

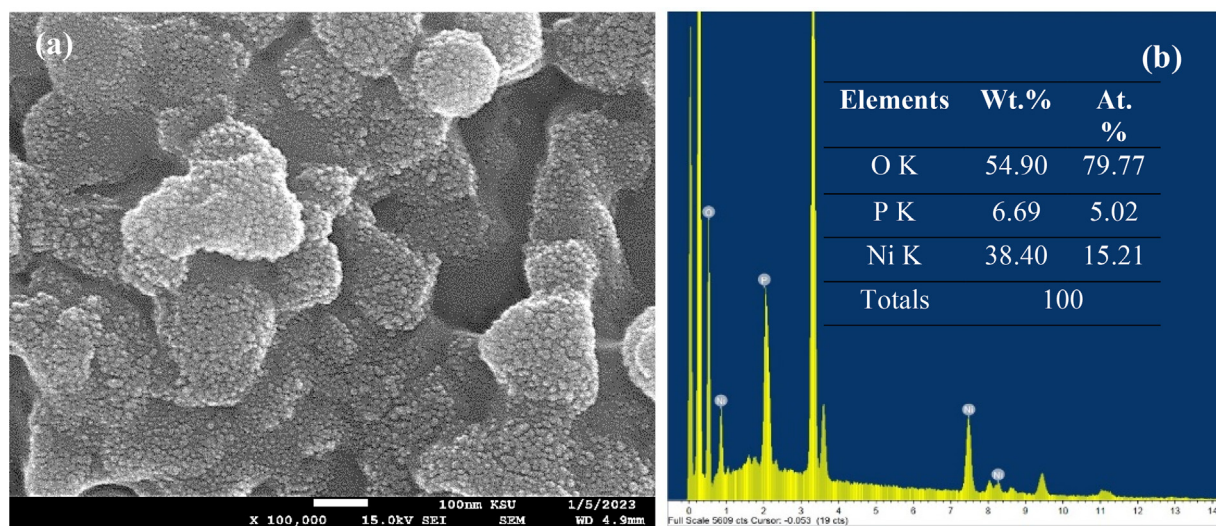


Fig. 7. (a) SEM image and (b) EDX and elemental analysis of *meso*-NiPO after being used in a long-term stability test for 3 h in in 0.33 M urea/2.0 M KOH solution at an oxidation potential of 0.6 V vs. Ag/AgCl.

Table 2

Comparison of electrochemical performance of *meso*-NiPO catalyst for UOR in alkaline solution with that reported in the literature relating to nickel-based electrocatalysts derived from CVs measurements.

Anodic materials	Onset potential (V)	Stability (min.)	specific activity, mA/cm ² , (mass activity, mA/cm ² mg)	Electrolyte	Ref.
<i>meso</i> -structure of NiPO	0.33 V vs. Ag/AgCl	~17	30 (600) at 0.5 V	0.10 M urea/ 1.0 M KOH	(Omar et al., 2016)
nickel phosphate nanorods	0.27 V vs. SCE	150	160	0.33 M urea/ 1.0 M KOH	(Pujari et al., 2021)
NiCoPO nanosheets	0.22 V vs. Ag/AgCl	30	65.4	0.10 M urea/ 1.0 M KOH	(Zhou et al., 2019)
Ni ₃ (PO ₄) ₂ ·8H ₂ O	0.45 V vs. Ag/AgCl	60	50	0.3 M urea/ 0.5 M KOH	(Vedharathinam and Botte, 2013)
Ni-WC/MWCNT	0.43 V vs. Hg/HgO	-	46.4	0.33 M urea/ 1.0 M KOH	(Touny and Saleh, 2018)
NiCo ₂ O ₄ nanowire/NF	0.19 V vs. Ag/AgCl	~27	570	0.33 M urea/ 5.0 M KOH	(Song et al., 2017)
3D porous NiO/NF	0.48 vs. Ag/AgCl		222	0.1 M urea/ 8.0 M NaOH	(Zhang et al., 2019)
Mesoporous Ni ₃ (PO ₄) ₂ nanoparticles	0.30 V vs. Ag/AgCl	180	141.4 (700.7) at 0.6 V	0.33 M urea/2.0 M KOH	This work

tion in alkaline solution (141.4 mA/cm², 700.7 mA/cm² mg) than the reported nickel phosphate-based catalysts with different nanoarchitectures such as NiPO (30 mA/cm², 600 mA/cm² mg) (Song et al., 2017), NiCoPO nanosheets (65.4 mA/cm²) (Yang et al., 2019), and Ni₃(PO₄)₂·8H₂O (50 mA/cm²) (Al-Omair et al., 2017). However, the *meso*-NiPO catalyst showed lower specific activity than NiCo₂O₄ nanowire/NF (570 mA/cm²) (Sha et al., 2019), the nickel phosphate nanorods/NF (160 mA/cm²) (Tsai et al., 2020), and 3D porous NiO/NF (222 mA/cm²) (Zhang et al., 2019) presumably because the later catalysts are deposited hydrothermally onto high surface area nickel foam substrates and high concentration of KOH electrolyte.

Finally, the hydrogen evolution rate (HER) during urea electrolysis at *meso*-NiPO catalyst was further monitored in 2.0 M KOH and 0.33 M urea solution using an H-shape electrolyzer (shown in Fig. S4 in supporting materials) assembled with *meso*-NiPO anode (0.50 mg/cm²) and nickel foam as the cathode. Fig. 8 shows the cathodic hydrogen production rate at different applied potentials of 1.6, 1.8 and 2.0 V using 2.0 M KOH solution in the absence

and presence of 0.33 M urea. The results show that in pure 2.0 M KOH solution and at an applied bias of 1.6 V, the rate of hydrogen generation at the cathode reaches about 38.5 μmol/h, while in the presence of 0.33 M urea, the hydrogen production rate has increased to about 100 μmol/h. This indicates that about 2.5 times more hydrogen production rate was obtained in the presence of urea. Moreover, the hydrogen production rate at the *meso*-NiPO anode was higher by more than four times compared to the *bare*-NiPO catalyst (about 23.0 μmol/h). As the applied potential further increases to 1.8 and 2.0 V, the rate of hydrogen evolution increases to 232 and 415 μmol/h respectively. The faradaic efficiency obtained using the *meso*-NiPO anode was found to equal 96.8%, indicating high energy efficiency and cheaper hydrogen green production using *meso*-NiPO catalyst and urea electrolysis.

4. Conclusion

The synthesis of *meso*-NiPO electrocatalyst using chemical deposition from a liquid crystal template has demonstrated great

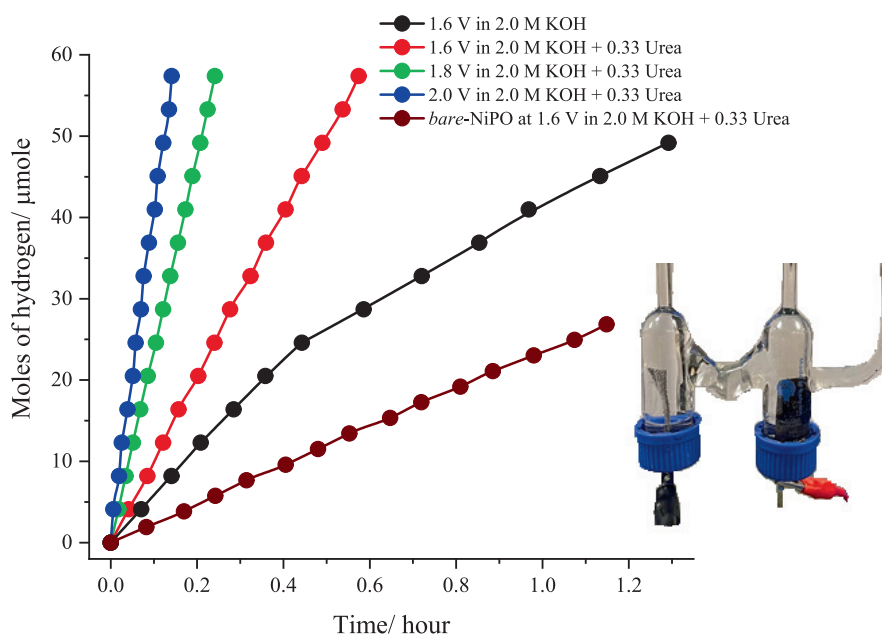


Fig. 8. Plot of the cathodic hydrogen production rate obtained using an H-shape electrolyzer and *meso*-NiPO anode (loading 0.50 mg/cm²) compared to *bare*-NiPO at a different applied potential of 1.6, 1.8 and 2.0 V using 2.0 M KOH solution in the absence and presence of 0.33 M urea. The inset shows the H-shape electrolyzer assembled with *meso*-NiPO anode (0.50 mg/cm²) and nickel foam as a cathode.

potential for enhancing the electro-oxidation of urea in alkaline solutions. Mesoporous nickel phosphate nanoparticles with a larger surface area and improved electrocatalytic performance for urea oxidation were prepared via simple chemical precipitation from the surfactant liquid crystal template media. The nickel ions dissolved in the aqueous domain of the hexagonal liquid crystalline phase of the Brij 78 template were reacted with sodium phosphate solution to precipitate the mesoporous nickel phosphate catalyst. The produced $\text{Ni}_3(\text{PO}_4)_2$ nanoparticles are an amorphous and highly porous structure with a specific surface area of $43.50 \text{ m}^2/\text{g}$ and exhibit significantly enhanced electrocatalytic performance and stability towards UOR. As compared with bare-NiPO, the *meso*-NiPO electrode achieved mass activity of $700.7 \text{ mA}/\text{cm}^2 \text{ mg}$, lower oxidation onset potential (0.30 V vs. Ag/AgCl), and lower charge transfer resistance (3.35Ω) at an oxidation potential of 0.6 V vs. Ag/AgCl . Using an H-shape urea electrolyser, the corresponding cathodic hydrogen Faradic efficiency was 96.8% and the production rate reached $415 \mu\text{mol}/\text{h}$ at an applied bias of 2.0 V . The high-performance activity of the *meso*-NiPO catalyst is credited to the intrinsic large specific surface area and mesoporous architecture that provide more active sites, efficient charge transfer, as well as mass transport of the electroactive species. The room temperature chemical deposition from a surfactant liquid crystal template is a simple one-pot synthesis method that can be applied to precipitate a wide range of mesoporous inorganic catalysts for application in electrochemical energy catalytic reactions.

Declaration of Competing Interest

The authors declare that they have no known competing financial interests or personal relationships that could have appeared to influence the work reported in this paper.

Acknowledgements

This project was funded by the National Plan for Science, Technology, and Innovation (MAARIFAH), King Abdulaziz City for Science and Technology, Kingdom of Saudi Arabia, Award Number 13-NAN-1309-02.

Appendix A. Supplementary material

Supplementary data to this article can be found online at <https://doi.org/10.1016/j.arabjc.2023.105266>.

References

- Al-Omar, M., Touny, A., Saleh, M., 2017. Reflux-based synthesis and electrocatalytic characteristics of nickel phosphate nanoparticles. *J. Power Sources* 342, 1032–1039.
- Al-Sharif, M., Arunachalam, P., Abiti, T., Amer, M., Al-Shalwi, M., Ghanem, M.A., 2020. Mesoporous cobalt phosphate electrocatalyst prepared using liquid crystal template for methanol oxidation reaction in alkaline solution. *Arab. J. Chem.* 13, 2873–2882.
- Aziam, H., Indris, S., Knapp, M., Ehrenberg, H., Saadoune, I., 2020. Synthesis, characterization, electrochemistry, and in situ X-ray diffraction investigation of $\text{Ni}_3(\text{PO}_4)_2$ as a negative electrode material for lithium-ion batteries. *ChemElectroChem* 15, 3866–3873.
- Babar, P., Patil, K., Lee, D.M., Karade, V., Gour, K., Pawar, S., Kim, J.H., 2021. Cost-effective and efficient water and urea oxidation catalysis using nickel-iron oxyhydroxide nanosheets synthesized by an ultrafast method. *J. Colloid Interface Sci.* 584, 760–769.
- Barakat, N.A.M., El-Newehy, M.H., Yasin, A.S., Ghouri, Z.K., Al-Dehay, S.S., 2016. Ni & Mn nanoparticles decorated carbon nanofibers as effective electrocatalyst for urea oxidation. *Appl. Catal. A* 510, 180–188.
- Boggs, B., King, R., Botte, G., 2009. Urea electrolysis: direct hydrogen production from urine. *Chem. Commun.* 32, 4859–4861.
- Deng, C., Toe, C.Y., Li, X., Tan, J., Yang, H., Hu, Q., Chuanxin, H., 2022. Earth-Abundant metal-based electrocatalysts promoted anodic reaction in hybrid water electrolysis for efficient hydrogen production: recent progress and perspectives. *Adv. Energy Mater.* 12, 2201047.
- Ding, R., Qi, L., Jia, M., Wang, H., 2014. Facile synthesis of mesoporous spinel NiCo_2O_4 efficient electrocatalysts for urea electro-oxidation. *Nanoscale* 6, 1369–1376.
- Ding, R., Li, X., Shi, W., Xu, Q., Wang, L., Jiang, H., Yang, Z., Liu, E., 2016a. Mesoporous Ni-P nanocatalysts for alkaline urea electrooxidation. *Electrochim. Acta* 222, 455–462.
- Ding, R., Xudong, L., Wei, S., Qilei, X., Luo, W., Haixia, J., Zeng, Y., Enhui, L., 2016b. Mesoporous Ni-P nanocatalysts for alkaline urea electrooxidation. *Electrochimica Acta* 222, 455–462.
- Ghanem, M.A., Al-Mayouf, A.M., Singh, J.P., Arunachalam, P., 2017. Concurrent deposition and exfoliation of nickel hydroxide nanoflakes using liquid crystal template and their activity for urea electrooxidation in alkaline medium. *Electrocatalysis* 8, 16–26.
- Hassaninejad-Darzi, S., Gholami-Esfdivajani, M., 2016. Electrocatalytic oxidation of ethanol using modified nickel phosphate nanoparticles and multi-walled carbon nanotubes paste electrode in alkaline media for fuel cell. *Int. J. Hydrogen Energy* 41, 20085–20099.
- Hopsort, G., Do Carmo, D.P., Latapie, L., Karine, L., Serrano, K.G., Tzedakis, T., 2023. Progress toward a better understanding of the urea oxidation by electromediation of Ni(III)/Ni(II) system in alkaline media. *Electrochim. Acta* 442, 141898.
- Hu, X., Zhu, J., Li, J., Wu, Q., 2020. Urea electrooxidation: current development and understanding of Ni-based catalysts. *ChemElectroChem* 7, 3211–3228.
- Klähn, M., Mathias, G., Kötting, C., Nonella, M., Schlitter, J., Gerwert, K., Tavan, P., 2004. IR spectra of phosphate ions in aqueous solution: predictions of a DFT/MM approach compared with observations. *Chem. A Eur. J.* 108, 6186–6194.
- Li, J., Wang, S., Sun, S., Wu, X., Zhang, B., Feng, L., 2022. A review of hetero-structured Ni-based active catalysts for urea electrolysis. *J. Mater. Chem. A* 10, 9308–9326.
- Liu, D., Liu, T., Zhang, L., Qu, F., Du, G., Asiri, A., Sun, X., 2017a. High-performance urea electrolysis towards less energy-intensive electrochemical hydrogen production using a bifunctional catalyst electrode. *J. Mater. Chem. A* 5, 3208–3213.
- Liu, T., Liu, D., Qu, F., Wang, D., Zhang, L., Ge, R., Hao, S., Ma, Y., Du, G., Asiri, A.M., Chen, L., Sun, X., 2017b. Enhanced electrocatalysis for energy-efficient hydrogen production over CoP catalyst with nonelectroactive Zn as a promoter. *Adv. Energy Mater.* 7, 1–8.
- Megia, P.J., Vizcaino, A.J., Calles, J.A., Carrero, A., 2021. Hydrogen production technologies: from fossil fuels toward renewable sources: a mini review. *Energy Fuels* 35, 16403–16415.
- Nwodo, I.C., Nkele, A.C., Obodo, R.M., Udeh, J.N., Ani, P.C., Chime, C.P., Maaza, M., Ezema, F.I., 2023. Synthesis and characterization of Co-precipitated nickel phosphate $[\text{Ni}_3(\text{PO}_4)_2]$ nanoparticles prepared at varying precursor concentrations. *J. Indian Chem. Soc.* 20, 101026.
- Omar, F., Numan, A., Duraisamy, N., Bashir, S., Ramesh, K., Ramesh, S., 2016. Ultrahigh capacitance of amorphous nickel phosphate for asymmetric supercapacitor applications. *RSC Adv.* 6, 76298–76306.
- Omar, F., Numan, A., Bashir, S., Duraisamy, N., Vikneswaran, R., Loo, Y.L., Ramesh, K., Ramesh, S., 2018. Enhancing rate capability of amorphous nickel phosphate supercapacitance electrode via composition with crystalline silver phosphate. *Electrochim. Acta* 273, 216–228.
- Pujari, S., Kadam, S., Ma, Y., Khalate, S., Katkar, P., Marje, S., Patil, U., 2021. Highly sensitive hydrothermally prepared nickel phosphate electrocatalyst as non-enzymatic glucose sensing electrode. *J. Porous Mater.* 28, 369–381.
- Qian, G., Chen, J., Luo, L., Zhang, H., Chen, W., Gao, Z., Yin, S., Tsiakaras, P., 2020. Novel bifunctional V_2O_3 nanosheets coupled with N-doped-carbon encapsulated Ni heterostructure for enhanced electrocatalytic oxidation of urea-rich wastewater. *ACS Appl. Mater. Interfaces.* 12, 38061–38069.
- Saravanakumar, B., Haritha, A., Ravi, G., Yuvakkumar, R., 2020. Synthesis of $\text{X}_3(\text{PO}_4)_2$ [X = Ni, Cu, Mn] nanomaterials as an efficient electrode for energy storage applications. *J. Nanosci. Nanotechnol.* 20, 2813–2822.
- Sha, L., Ye, K., Wang, G., Shao, J., Zhu, K., Cheng, K., Yan, J., Wang, G., Cao, D., 2019. Hierarchical NiCo_2O_4 nanowire array supported on Ni foam for efficient urea electrooxidation in alkaline medium. *J. Power Sources* 412, 265–271.
- Shen, F., Jiang, W., Qian, G., Chen, W., Zhang, H., Luo, L., Yin, S., 2020. Strongly coupled carbon encapsulated Ni-WO₂ hybrids as efficient catalysts for water-to-hydrogen conversion via urea electro-oxidation. *J. Power Sources* 458, 228014.
- Sing, K., Everett, D., Haul, R., Moscou, L., Pierotti, R., Rouquerol, J., Siemieniowska, T., 1985. Reporting physisorption data for gas/solid systems with special reference to the determination of surface area and porosity. *Pure Appl. Chem.* 57, 603–619.
- Singh, R., Devavaraprasad, R., Kar, T., Chakraborty, A., Neergat, M., 2015. Electrochemical impedance spectroscopy of oxygen reduction reaction (ORR) in a rotating disk electrode configuration: effect of ionomer content and carbon-support. *J. Electrochem. Soc.* 162, F489–F498.
- Song, X., Gao, L., Li, Y., Chen, W., Mao, L., Yang, J.H., 2017. Nickel phosphate-based materials with excellent durability for urea electro-oxidation. *Electrochim. Acta* 251, 284–292.
- Sun, C.B., Guo, M.W., Siwal, S.S., Zhang, Q.B., 2020. Efficient hydrogen production via urea electrolysis with cobalt doped nickel hydroxide-riched hybrid films: Cobalt doping effect and mechanism aspect. *J. Catal.* 381, 454–461.
- Sun, H., Zhang, W., Li, J., Li, Z., Ao, X., Xue, K., Ken, K., Tang, J., Wang, C., 2021. Rh-engineered ultrathin NiFe-LDH nanosheets enable highly-efficient overall water splitting and urea electrolysis. *Appl. Catal. B Environ.* 284, 119740.

- Touny, A., Saleh, M., 2018. Enhanced methanol oxidation on nanoporous nickel phosphate modified platinum electrode in alkaline solution. *Int. J. Electrochem. Sci.* 13, 1042–1050. <https://doi.org/10.20964/2018.01.55>.
- Tsai, Y., Wu, M., 2020. Zeolitic nickel phosphate nanorods with open-framework structure (VSB-5) for catalytic application in electro-oxidation of urea. *Appl. Surf. Sci.* 529, 147175.
- Vedharathinam, V., Botte, G., 2012. Understanding the electro-catalytic oxidation mechanism of urea on nickel electrodes in alkaline medium. *Electrochim. Acta* 81, 292–300.
- Vedharathinam, V., Botte, G., 2013. Direct evidence of the mechanism for the electro-oxidation of urea on Ni(OH)₂ catalyst in alkaline medium. *Electrochim. Acta* 108, 660–665.
- Wu, N., Guo, R., Zhang, X., Gao, N., Chi, X., Cao, D., Hu, T., 2021. Nickel/nickel oxide nanocrystal nitrogen-doped carbon composites as efficient electrocatalysts for urea oxidation. *J. Alloys Compounds* 870, <https://doi.org/10.1016/j.jallcom.2021.159408> 159408.
- Wu, T.H., Lin, Y.C., Hou, B.W., Liang, W.Y., 2020. Nanostructured β-NiS catalyst for enhanced and stable electro-oxidation of urea. *Catalysts* 10, 1–11.
- Xie, L., Liu, Q., Luo, Y., Liu, Z., Xu, Y., Asiri, A.M., Sun, X., Xie, F., 2017. Bimetallic NiCoP nanosheets array for high-performance urea electro-oxidation and less energy-intensive electrolytic hydrogen production. *ChemistrySelect* 2, 10285–10289.
- Xie, J., Qu, H., Lei, F., Peng, X., Liu, W., Gao, L., Hao, P., 2018. Partially amorphous nickel-iron layered double hydroxide nanosheet arrays for robust bifunctional electrocatalysis. *J. Mater. Chem. A* 6, 16121–16129.
- Yan, W., Wang, D., Botte, G.G., 2012. Electrochemical decomposition of urea with Ni-based catalysts. *Appl Catal B* 127, 221–226.
- Yan, W., Wang, D., Diaz, L., Botte, G., 2014. Nickel nanowires as effective catalysts for urea electro-oxidation. *Electrochim. Acta* 134, 266–271.
- Yang, J., Song, X., Zhao, X., Wang, Y., Yang, Y., Gao, L., 2019. Nickel phosphate materials regulated by doping cobalt for urea and methanol electro-oxidation. *Int. J. Hydrogen Energy* 44, 16305–16314.
- Ye, K., Zhang, D., Guo, F., Cheng, K., Wang, G., Cao, D., 2015. Highly porous nickel@carbon sponge as a novel type of three-dimensional anode with low cost for high catalytic performance of urea electro-oxidation in alkaline medium. *J. Power Sources* 283, 408–415.
- Ye, K., Wang, G., Cao, D., Wang, G., 2018. Recent advances in the electro-oxidation of urea for direct urea fuel cell and urea electrolysis. *Top. Curr. Chem.* 376, 1–38.
- Zhang, D., Zhang, J., Wang, H., Cui, C., Jiao, W., Gao, J., Liu, Y., 2019. Novel Ni foam-based nickel oxalate-derived porous NiO nanostructures as highly efficient electrodes for the electrooxidation of methanol/ethanol and urea. *J. Alloys and Compounds* 806, 1419–1429.
- Zhou, Y., Liu, C., Li, X., Sun, L., Wu, D., Li, J., Huo, P., Wang, H., 2019. Chemical precipitation synthesis of porous Ni₂P₂O₇ nanowires for supercapacitor. *J. Alloy. Compd.* 790, 36–41.
- Zhu, B., Liang, Z., Zou, R., 2020. Designing advanced catalysts for energy conversion based on urea oxidation reaction. *Small*. 16, 1906133 (1–19).